

Clinically-Grounded Counterfactual Reasoning for Medical Video Diagnosis

Jianzhe Gao² Churan Wang¹✉ Weiyi Zhang³✉ Jianghua Li³ Li-An Li³
Wenguan Wang²✉ Yixin Zhu^{5,7,8,9} Yizhou Wang^{4,6,7}

<https://gaozzz.github.io/MedVCR/>

¹ Center for Data Science in Clinical Medicine, Peking University Third Hospital

² The State Key Lab of Brain-Machine Intelligence, Zhejiang University

³ Department of Gynecology and Obstetrics, 7th Medical Center of Chinese PLA General Hospital

⁴ School of Computer Science, Peking University ⁵ School of Psychological and Cognitive Sciences, Peking University

⁶ State Key Lab of General AI, Peking University ⁷ Nat'l Eng. Research Center of Visual Technology

⁸ Beijing Key Laboratory of Behavior and Mental Health, Peking University

⁹ Embodied Intelligence Lab, PKU-Wuhan Institute for Artificial Intelligence

Abstract

Clinical video diagnosis, in which physicians assess dynamic tissue responses across procedural stages, is critical for detecting diseases such as cervical and colorectal cancers. Recent spatiotemporal models map visual progressions directly to diagnostic outputs, yet overlook two hallmarks of expert reasoning: clinically grounded diagnostic principles and hypothesis-driven counterfactual thinking. This gap leads existing methods to conflate causal pathological cues with non-pathological variations, thereby limiting their reliability in data-scarce settings. Here we show that explicitly modeling counterfactual tissue evolution, guided by clinical rules that encode expert diagnostic principles, substantially improves diagnostic robustness—emulating the hypothesis-driven reasoning clinicians employ in practice. We introduce **MEDVCR**, comprising a Counterfactual Generator (CG) that synthesizes hypothetical tissue transitions via diffusion modeling, a Counterfactual Representation Learning (CRL) module that enforces temporal consistency, pathological separability, and counterfactual alignment, and a Dual Diagnostic Prediction (DDP) strategy that combines video-level context with frame-level counterfactual contrast. On two representative tasks, **MEDVCR** achieves 93.0% Recall@1 on colonoscopy (+10.2%) and 94.8% Average Precision (AP) on colonoscopy (+2.6%), outperforming all state-of-the-art (SOTA) baselines. We anticipate that this counterfactual reasoning paradigm will open new avenues for vision-based clinical diagnostic tasks toward more transparent and interpretable decision support.

1. Introduction

Clinical diagnosis in many diseases relies on video-level examinations, where physicians assess how tissue appearance evolves across procedural stages to determine un-

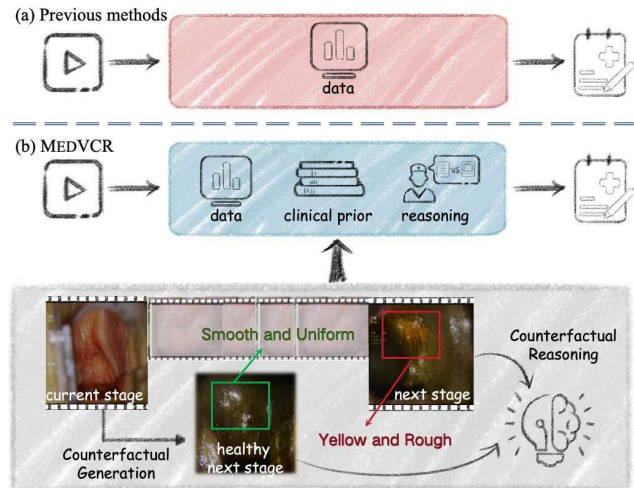


Figure 1. **Motivation and overview of MEDVCR.** (a) Previous methods fall into the data-driven paradigm that directly maps observations to diagnostic outputs. (b) The proposed **MEDVCR** incorporates clinical rules and models tissue evolution under different disease states. It performs counterfactual reasoning by contrasting factual observations with hypothetical alternatives to support reliable diagnosis.

derlying pathology [26, 35, 55]. This diagnostic process is often time-consuming, highly subjective, and operator-dependent, making automated medical video diagnosis increasingly valuable in clinical practice [11, 39]. Recent advances in video understanding have enabled end-to-end learning for medical video analysis [28, 29, 50], with mainstream methods leveraging convolution- or self-attention-based visual encoders [59, 80] to achieve promising performance in colonoscopy polyp detection [14, 42], laparoscopic surgery phase recognition [15, 23, 39], and fetal ultrasound standard plane localization [11, 25, 46].

Despite these advances, three fundamental challenges remain unresolved. **(i) Misinterpreting pathological evolution.** Prevailing models treat medical videos as sequences

of visual changes [70, 79], analyzing pixel-level variations while overlooking how tissues evolve across examination stages (*e.g.*, the transient reactions to acetic acid or iodine). **(ii) Ignoring clinical diagnostic principles.** Relying purely on data-driven optimization without embedding explicit clinical knowledge [30, 74], most existing methods are prone to conflating meaningful diagnostic cues with non-pathological variations from illumination shifts, reagent color variations, or camera motion. **(iii) Lacking hypothesis-driven reasoning.** Rather than distinguishing causal pathological cues from incidental correlations [9, 67], current models simply correlate observed patterns with diagnostic outputs. This stands in contrast to clinicians, who mentally simulate “What if this tissue were benign instead of malignant?” and compare hypothetical scenarios against observed reality—a counterfactual reasoning capacity, essential yet absent in most automated systems.

This hypothesis-driven reasoning is especially critical when learning from limited clinical cases [9]. In practice, clinicians routinely simulate alternative pathological scenarios and contrast these hypothetical evolutions against actual tissue progressions [53]. Through such counterfactual thinking, they extract generalizable diagnostic cues from sparse examples and separate true pathological signals from confounding factors—a capability that current automated methods notably lack. Addressing these challenges calls for a unified framework that simultaneously models pathology-conditioned tissue evolution, encodes clinical diagnostic principles as explicit constraints, and performs contrastive reasoning over factual and hypothetical observations—mirroring the cognitive process clinicians employ in practice.

To address these challenges, we propose **MEDVCR**, a hypothesis-driven counterfactual reasoning framework for medical video diagnosis that emulates clinical diagnostic thinking. As illustrated in Fig. 1, **MEDVCR** integrates factual observations with clinically plausible hypothetical scenarios to simulate real-world diagnostic reasoning. It consists of three components. A CG (Sec. 3.1) synthesizes realistic tissue transitions across clinical stages under specified pathological states via diffusion-based modeling. A CRL module (Sec. 3.2) learns spatiotemporal representations regularized by three clinical rules: *temporal consistency* across examination stages, *pathological separability* between disease patterns, and *counterfactual alignment* with plausible pathological explanations. A DDP strategy (Sec. 3.3) aggregates global temporal dynamics while contrasting factual observations against counterfactual scenarios to yield reliable and interpretable predictions.

MEDVCR is evaluated under two representative settings. In fully supervised colposcopy biopsy-site localization, **MEDVCR** achieves 93.0% Recall@1, exceeding the best prior method by 10.2%. In weakly supervised

colonoscopy polyp-frame detection, it attains 94.8% AP, surpassing the strongest baseline by 2.6%. Extensive ablation studies further validate each component’s contribution.

2. Related Work

Medical video diagnosis Early methods [33, 64, 65] apply frame-level CNNs that analyze each frame independently, neglecting the temporal evolution of tissue responses throughout examination. With the emergence of spatiotemporal backbones such as I3D [8], SlowFast [21], and ViViT [1], the field shifted toward end-to-end models that jointly capture spatial appearance and temporal progression. These backbones were first adopted for surgical phase recognition [15, 19, 33, 90], then extended to finer-grained surgical video analysis incorporating tool usage cues and instrument–tissue interactions [12, 34, 54, 60]. Parallel lines of work address medical video segmentation for precise lesion boundary delineation [10, 14, 16, 37, 80] and weakly supervised video detection that identifies pathological frames using only video-level labels [44, 47, 62]. More recently, foundation models have extended the scope to high-complexity data such as whole-slide pathology images [75] and multimodal clinical contexts [85]. Despite these advances, these methods focus primarily on observable visual variations and lack counterfactual reasoning—contradicting the clinical principle of determining pathology by mentally comparing observed tissue responses with hypothetical alternatives. **MEDVCR** addresses this gap by explicitly simulating and contrasting tissue evolution under different pathological conditions.

Counterfactual reasoning Counterfactual reasoning, a cornerstone of causal inference and decision-making, enables models to explore hypothetical scenarios by predicting alternative outcomes under modified conditions [2, 32, 36, 56, 58, 69, 72]. Early approaches integrate Structural Causal Models with deep generative architectures, leveraging normalizing flows and variational inference to infer exogenous noise under the no-unobserved-confounders assumption [31, 45, 51, 78]. GAN-based methods perform counterfactual inference through adversarial objectives or reparameterized attribute distributions to model interventional effects on image semantics [13, 24, 67, 88], while VAE-based frameworks learn structured latent spaces that capture causal dependencies among high-level factors [5, 77]. More recently, diffusion models learn causal paths between semantic attributes or scene configurations by formulating noise abduction as a forward diffusion process [38, 43, 84]. Recent work has adapted these ideas to medical image analysis, using counterfactual generation to enhance diagnostic interpretability, data diversity, and model reliability [81]. **MEDVCR** extends this paradigm to medical video diagnosis, enabling counterfactual reasoning over temporal tissue transitions across examination stages.

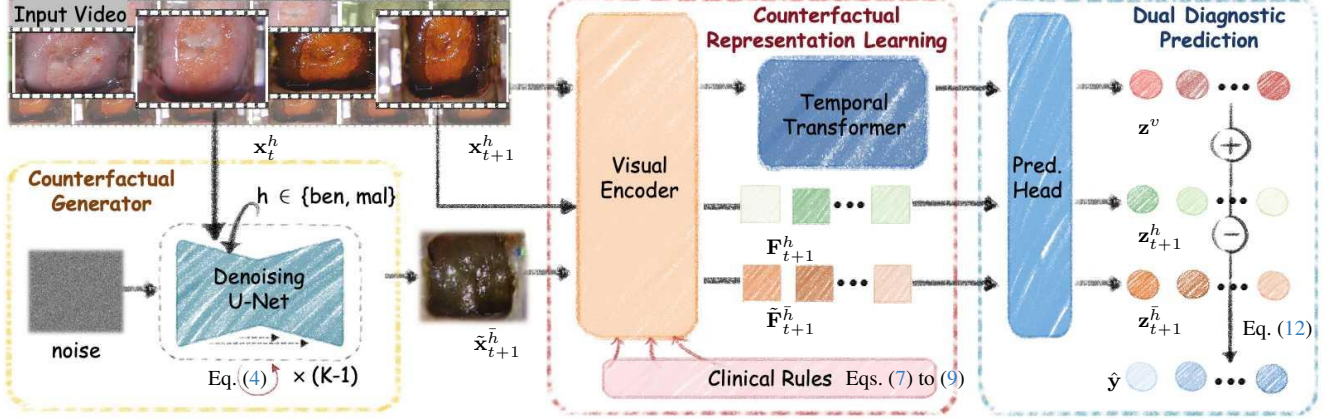


Figure 2. **Overview of MEDVCR.** Given a medical video sequence, the CG (Sec. 3.1) synthesizes alternative tissue transitions under benign/malignant hypotheses. The CRL module (Sec. 3.2) encodes factual and counterfactual frames, enforcing clinical rules for temporal consistency, pathological separability, and counterfactual alignment. The DDP strategy (Sec. 3.3) then integrates temporal context with frame-level counterfactual contrast to produce diagnoses.

3. Method

Problem formulation Medical video analysis aims to infer diagnostic cues that reflect the underlying pathological condition and its temporal evolution. Given a video sequence $\mathcal{V} = \{\mathbf{x}_t\}_{t=1}^T$ recording progressive tissue changes across examination stages, each frame \mathbf{x}_t is influenced by its stage s_t , the latent health state $h \in \{\text{benign, malignant}\}$, and nuisance factors such as illumination or camera motion. The objective is to produce clinically meaningful predictions $\hat{\mathbf{y}} \in [0, 1]^P$, where P denotes the number of prediction points that highlight diagnostically significant regions or potential sampling sites.

Overall design (Fig. 2) MEDVCR integrates counterfactual reasoning with medical video diagnosis to enhance diagnostic reliability. Specifically, a pretrained CG (Sec. 3.1) synthesizes alternative tissue transitions that serve as counterfactual supervision. Through CRL (Sec. 3.2), spatiotemporal representations are captured and regularized by three clinical rules. The learned representations are then fed into a DDP strategy (Sec. 3.3) that integrates global temporal context with localized counterfactual evidence for final diagnosis.

3.1. Counterfactual Generator (CG)

Physicians diagnose not only by observing how tissue appearance evolves across examination stages, but also by mentally comparing the observed progression with alternative outcomes under different pathological states—an implicit counterfactual reasoning process. Inspired by this, CG is designed to synthesize realistic tissue transitions conditioned on specified health conditions.

Formally, the generator \mathcal{G} is formulated as a conditional diffusion model. Given a reference frame \mathbf{x}_t from stage s_t and a target health condition h , \mathcal{G} generates the corresponding frame $\tilde{\mathbf{x}}_{t+1}^h$ at the subsequent stage s_{t+1} by estimating

the expected tissue appearance under the specified pathological state. The generative process comprises three components: a fixed *forward diffusion* that corrupts real tissue frames, a learnable *reverse denoising* that restores diagnostic information, and an iterative *sampling process* that synthesizes tissue transitions conditioned on any health state.

Forward diffusion The forward process follows a fixed Markov chain that progressively corrupts the target frame \mathbf{x}_{t+1} by adding Gaussian noise across K diffusion steps:

$$q(\epsilon_k | \mathbf{x}_{t+1}) = \mathcal{N}(\epsilon_k; \sqrt{\alpha_k} \mathbf{x}_{t+1}, (1 - \alpha_k) \mathbf{I}), \quad (1)$$

where $k \in \{1, \dots, K\}$, $\bar{\alpha}_k = \prod_{i=1}^k \alpha_i$ denotes the cumulative noise schedule, and ϵ_k represents the progressively noised frame at diffusion step k . As k increases, the tissue structure and color cues are gradually replaced by random noise, yielding a fully stochastic signal at the final step K . This diffusion process defines the degradation trajectory that the reverse model later learns to invert.

Reverse denoising This process learns to iteratively recover the clean frame from its noisy counterpart through a parameterized conditional transition. At each diffusion step k , a U-shaped network \mathcal{F}^u predicts the step-specific noise component $\hat{\epsilon}_k$ from the current noisy input ϵ_k :

$$\hat{\epsilon}_k = \mathcal{F}^u(\epsilon_k, \mathbf{x}_t, h, k). \quad (2)$$

Here, both ϵ_k and \mathbf{x}_t are encoded by the same visual backbone to extract spatial context, h is projected into a latent vector that modulates pathological manifestation, and k is embedded via sinusoidal positional encoding to represent diffusion progress. Following the standard DDPM denoising formulation [57], the predicted noise $\hat{\epsilon}_k$ is removed to obtain a cleaner estimate at the previous step:

$$\epsilon_{k-1} = \frac{1}{\sqrt{\alpha_k}} \left(\epsilon_k - \frac{\beta_k}{\sqrt{1 - \alpha_k}} \hat{\epsilon}_k \right), \quad (3)$$

where α_k and β_k define the predefined noise schedule controlling the denoising rate. This process gradually restores spatial structures and chromatic patterns coherent with the specified pathological condition.

Sampling process Built upon the learned denoising process, the generator \mathcal{G} synthesizes tissue appearances under different pathological conditions. Starting from Gaussian noise $\epsilon_k \sim \mathcal{N}(0, \mathbf{I})$, \mathcal{G} iteratively applies \mathcal{F}^u across k steps to reconstruct the tissue frame:

$$\tilde{\mathbf{x}}_{t+1}^h = \mathcal{G}(\mathbf{x}_t, h) = \mathcal{F}^{u,1:k}(\epsilon_k; \mathbf{x}_t, h), \quad (4)$$

where $\mathcal{F}^{u,1:k}$ denotes the sequential composition of all denoising steps from k to 1. This iterative process transforms random noise into a coherent tissue image whose structure and color patterns evolve consistently with the specified health condition h . Generating both benign and malignant variants enables the model to simulate alternative diagnostic trajectories for counterfactual reasoning.

3.2. Counterfactual Representation Learning

Given the pretrained \mathcal{G} , the medical video learner is trained to extract spatiotemporal representations from both factual video sequences and counterfactual hypotheses. A set of clinical rules is further introduced to enforce expected invariances and separabilities across temporal and pathological dimensions, encouraging the learner to derive representations that are both physiologically coherent and diagnostically interpretable.

Medical video learner The learner consists of a visual encoder \mathcal{F}^e and a temporal Transformer \mathcal{F}^t , forming a hierarchical architecture for spatiotemporal representation learning. Given a video sequence $\mathcal{V} = \{\mathbf{x}_t\}_{t=1}^T$, overlapping clips of length L are extracted with a temporal stride to preserve continuity, yielding a set of clips $\{\mathcal{C}_i\}_{i=1}^C$, where each clip $\mathcal{C}_i = \{\mathbf{x}_t\}_{t=i}^{i+L-1}$. Each clip is processed by \mathcal{F}^e (i.e., I3D [8]) to obtain frame-level embeddings:

$$\mathbf{F}_i^e = \mathcal{F}^e(\mathcal{C}_i) \in \mathbb{R}^{L \times d}. \quad (5)$$

Here, each row of \mathbf{F}_i^e corresponds to a frame representation and d denotes the feature dimension. All \mathbf{F}_i^e are concatenated into a unified temporal sequence $\mathbf{F}^e \in \mathbb{R}^{(C \cdot L) \times d}$. A learnable temporal token $\mathbf{F}^\tau \in \mathbb{R}^d$ is then prepended to \mathbf{F}^e , enabling the learner to aggregate stage-wise dynamics across the full sequence. The resulting sequence is fed into \mathcal{F}^t to capture long-range dependencies:

$$\mathbf{F}^v = \mathcal{F}^t([\mathbf{F}^\tau, \mathbf{F}^e]) \in \mathbb{R}^{(C \cdot L + 1) \times d}, \quad (6)$$

where $[\cdot, \cdot]$ denotes concatenation. The final representation \mathbf{F}^v encodes both local frame-wise patterns and global progression dynamics across examination stages.

Clinical rules Physiological and diagnostic knowledge is incorporated into representation learning through three clinical rules. Each rule is formulated using frame

pairs $(\mathbf{x}_t, \mathbf{x}_{t+1})$ and counterfactual frames $\tilde{\mathbf{x}}_{t+1}^h$. Specifically, the pairs $(\mathbf{x}_t, \mathbf{x}_{t+1})$ represent consecutive examination stages (s_t, s_{t+1}) of the same tissue region, and the counterfactual frame $\tilde{\mathbf{x}}_{t+1}^h$ is generated by \mathcal{G} from \mathbf{x}_t under health condition $h \in \{\text{benign, malignant}\}$ to model alternative diagnostic outcomes. All frames are encoded by \mathcal{F}^e to obtain representations $\{\mathbf{F}_t, \mathbf{F}_{t+1}, \tilde{\mathbf{F}}_{t+1}^{\text{ben}}, \tilde{\mathbf{F}}_{t+1}^{\text{mal}}\}$, where $\tilde{\mathbf{F}}$ denotes features extracted from counterfactual frames $\tilde{\mathbf{x}}$.

Rule 1: Temporal consistency. Pathological status remains stable throughout medical examination sequences. The same tissue region, whether benign or malignant, maintains its diagnostic identity across different examination stages, despite variations in appearance due to reagent reactions, illumination differences, or procedural manipulation.

This rule implies that the diagnostic information encoded in features should remain consistent across examination stages for the same tissue region. In information-theoretic terms, the encoder is expected to preserve health-related information while suppressing correlations with stage-dependent factors:

$$\mathcal{M}(\mathbf{F}_t; h) \approx \mathcal{M}(\mathbf{F}_{t+1}; h) \gg \mathcal{M}(\mathbf{F}_t, \mathbf{F}_{t+1}; s_t, s_{t+1}), \quad (7)$$

where $\mathcal{M}(X; Y)$ denotes the mutual information between random variables X and Y , and s_t, s_{t+1} denote the corresponding examination stages. This relation ensures that the representations retain diagnostic information while remaining invariant to stage-specific variations.

Rule 2: Pathological separability. Benign and malignant tissues arise from distinct biological processes and exhibit discernible morphological and chromatic signatures.

This rule enforces a clear separation of pathological conditions in the latent representation space. From an information-theoretic perspective, the features should collectively provide strong diagnostic information while remaining independent across pathological categories:

$$\mathcal{M}(h; \mathbf{F}_{t+1}^{\text{ben}}) + \mathcal{M}(h; \mathbf{F}_{t+1}^{\text{mal}}) \gg \mathcal{M}(\mathbf{F}_{t+1}^{\text{ben}}; \mathbf{F}_{t+1}^{\text{mal}}). \quad (8)$$

The left-hand terms encourage each pathological representation to preserve strong diagnostic dependency on h , while the right-hand term penalizes mutual dependence between benign and malignant features, ensuring a well-separated and clinically interpretable latent space.

Rule 3: Counterfactual alignment. Clinical diagnosis relies on the concordance between observed tissue characteristics and the expected manifestations of the true pathological state, while maintaining clear divergence from those associated with alternative conditions.

This rule requires the encoder to align factual observations with their pathology-consistent counterfactual counterparts while separating them from incompatible ones. Formally:

$$\mathcal{M}(\mathbf{F}_{t+1}^h; \tilde{\mathbf{F}}_{t+1}^h) \gg \mathcal{M}(\mathbf{F}_{t+1}^h; \tilde{\mathbf{F}}_{t+1}^{\bar{h}}), \quad (9)$$

where \bar{h} denotes the opposite health state. This relation enforces diagnostic alignment with the true pathology while suppressing agreement with incompatible assumptions, thereby promoting clinically coherent counterfactual reasoning in the learned representation space.

3.3. Dual Diagnostic Prediction (DDP)

Clinical diagnosis follows a hierarchical reasoning process: physicians evaluate the entire examination video to assess global tissue response patterns while simultaneously examining individual keyframes to identify localized pathological evidence. Motivated by this, DDP strategy integrates video-level temporal context with frame-level counterfactual analysis for comprehensive diagnostic predictions.

Video-level assessment The entire examination sequence \mathcal{V} is processed by the medical video learner to obtain the video-level feature \mathbf{F}^v (Eq. (6)), which is subsequently passed through the prediction head \mathcal{F}^p to yield logits \mathbf{z}^v :

$$\mathbf{z}^v = \mathcal{F}^p(\mathbf{F}^v) \in \mathbb{R}^P, \quad (10)$$

where P is the number of diagnostic outcomes.

Frame-level analysis To capture localized pathological evidence, both the factual keyframe \mathbf{x}_{t+1}^h and its counterfactual counterpart $\tilde{\mathbf{x}}_{t+1}^{\bar{h}}$ are independently analyzed to provide complementary diagnostic perspectives:

$$\mathbf{z}_{t+1}^h = \mathcal{F}^p(\mathcal{F}^e(\mathbf{x}_{t+1}^h)), \quad \mathbf{z}_{t+1}^{\bar{h}} = \mathcal{F}^p(\mathcal{F}^e(\tilde{\mathbf{x}}_{t+1}^{\bar{h}})), \quad (11)$$

where $\mathbf{z}_{t+1}^h, \mathbf{z}_{t+1}^{\bar{h}} \in \mathbb{R}^P$ represent per-site diagnostic logits from the factual and counterfactual analyses, respectively.

Diagnostic fusion The final prediction integrates global temporal context with localized counterfactual contrast:

$$\hat{\mathbf{y}} = \mathcal{F}^\sigma(\mathbf{z}^v + \mathbf{z}_{t+1}^h - \mathbf{z}_{t+1}^{\bar{h}}) \in [0, 1]^P, \quad (12)$$

where $\mathcal{F}^\sigma(\cdot)$ denotes the element-wise sigmoid function, producing independent probabilities for each diagnostic outcome. This formulation combines video-level progression dynamics \mathbf{z}^v with frame-level evidence \mathbf{z}_{t+1}^h supporting the true pathology, while simultaneously suppressing cues aligned with the alternative hypothesis $\mathbf{z}_{t+1}^{\bar{h}}$, thereby realizing differential diagnostic reasoning at the prediction level.

3.4. Hybrid Loss Function

The generator \mathcal{G} is first pretrained to produce counterfactual supervision. Subsequently, the medical video learner and diagnostic head are jointly optimized to ensure physiologically consistent and diagnostically faithful predictions.

Generator loss The generator \mathcal{G} is trained to reconstruct pathology-consistent frames through a denoising diffusion process. At each diffusion step k , the U-shaped denoising network \mathcal{F}^u predicts the noise component $\hat{\epsilon}_k$ from the current noisy input ϵ_k , conditioned on \mathbf{x}_t and $h \in \{\text{benign}, \text{malignant}\}$. The generator objective minimizes

the expected mean-squared discrepancy between the predicted and reference noise across diffusion timesteps:

$$\mathcal{L}^{\text{gen}} = \mathbb{E}_{\mathbf{x}_t, \mathbf{x}_{t+1}, h, k} [\|\epsilon_k - \hat{\epsilon}_k\|_2^2], \quad (13)$$

where $\hat{\epsilon}_k = \mathcal{F}^u(\epsilon_k, \mathbf{x}_t, h, k)$ (Eq. (2)). This encourages \mathcal{G} to synthesize temporally coherent tissue transitions under the specified pathological condition.

Visual encoder loss All clinical rule constraints are imposed on frame-level embeddings extracted by the visual encoder \mathcal{F}^e , ensuring physiologically consistent representations before temporal aggregation by \mathcal{F}^t .

To maintain diagnostic stability across consecutive stages (Rule 1), a temporal contrastive loss encourages representations from adjacent stages to remain consistent:

$$\mathcal{L}^{\text{temp}} = 1 - \mathcal{F}^{\text{sim}}(\mathbf{F}_t^h, \mathbf{F}_{t+1}^h), \quad (14)$$

where $\mathcal{F}^{\text{sim}}(\cdot, \cdot)$ denotes normalized cosine similarity.

To encourage discriminative encoding of pathological states (Rule 2), a soft separability loss guides representations to reflect diagnostic differences:

$$\mathcal{L}^{\text{sep}} = \mathcal{F}^{\text{sim}}(\mathbf{F}_{t+1}^h, \mathbf{F}_t^h) - \mathcal{F}^{\text{sim}}(\mathbf{F}_{t+1}^h, \tilde{\mathbf{F}}_{t+1}^{\bar{h}}). \quad (15)$$

To ensure alignment between factual and counterfactual reasoning (Rule 3), a counterfactual alignment loss adopts a triplet formulation that pulls features toward their pathology-consistent counterparts while pushing them away from incompatible ones:

$$\mathcal{L}^{\text{align}} = \max(0, m + \mathcal{F}^{\text{sim}}(\mathbf{F}_{t+1}^h, \tilde{\mathbf{F}}_{t+1}^{\bar{h}}) - \mathcal{F}^{\text{sim}}(\mathbf{F}_{t+1}^h, \tilde{\mathbf{F}}_{t+1}^h)), \quad (16)$$

where m denotes the margin governing alignment strength.

Diagnostic loss The diagnostic head is optimized using a supervised objective that compares the predicted probabilities $\hat{\mathbf{y}}$ with the ground-truth labels $\mathbf{y} \in \{0, 1\}^P$:

$$\mathcal{L}^{\text{diag}} = -\frac{1}{P} \sum_{k=1}^P [y_k \log \hat{y}_k + (1 - y_k) \log(1 - \hat{y}_k)]. \quad (17)$$

3.5. Implementation Details

Training All experiments are implemented in PyTorch and trained on a single NVIDIA RTX 4090 GPU with batch size 8. The CG adopts a U-Net backbone with diffusion timesteps $K=1000$, trained for 20k iterations using AdamW with a cosine learning rate schedule and a base learning rate of 10^{-4} . The visual encoder \mathcal{F}^e is initialized from pretrained I3D [8]. Images are resized to 256×256 across all tasks. Please refer to Sec. A for more details.

Inference During inference, the input video sequence \mathcal{V} is divided into overlapping clips and encoded by \mathcal{F}^e to obtain global spatiotemporal representations. For frame-level diagnostic reasoning, we follow standard clinical screening protocols where observed tissues are treated as suspected cases ($h=\text{mal}$) to enable falsification. Accordingly, the counterfactual target is set to benign ($\bar{h}=\text{ben}$). To

obtain the counterfactual reference for the current frame \mathbf{x}_t , the generator \mathcal{G} uses the preceding frame \mathbf{x}_{t-1} to synthesize the benign estimate $\tilde{\mathbf{x}}_t^h$. Finally, DDP module computes the diagnostic probabilities $\hat{\mathbf{y}}$ by integrating the video-level temporal context with the contrastive features derived from the pair $(\mathbf{x}_t, \tilde{\mathbf{x}}_t^h)$.

4. Experiments

To demonstrate the versatility and effectiveness of **MEDVCR**, experiments are conducted under two representative supervision settings reflecting common clinical video analysis scenarios: **fully supervised learning** (Sec. 4.1) with detailed frame-level pathological annotations, and **weakly supervised learning** (Sec. 4.2) using only video-level diagnostic labels. Each setting addresses clinically significant tasks embodying typical challenges, while ablation studies (Sec. 4.3) systematically analyze individual component contributions. Additional validation on medical image analysis is provided in Sec. B.

4.1. Fully Supervised Medical Video Diagnosis

To evaluate **MEDVCR** under the fully supervised setting, biopsy-site localization in colposcopy videos is adopted as the representative task. Since biopsy sites lie on fixed clock-face positions, this task is formulated as a multi-label classification problem.

Task description Colposcopy is a standard gynecological procedure for cervical cancer prevention and early detection [76]. During the examination, a colposcope equipped with a magnified optical system is positioned outside the vagina to observe the cervical epithelium under different reagents such as saline, acetic acid, and iodine solution [6]. These reagents induce transient color and texture changes that help reveal abnormal epithelial patterns and potential precancerous lesions. The analysis of colposcopy videos focuses on identifying regions of clinical interest for biopsy.

Dataset The in-house dataset comprises 623 patient-specific colposcopy examination records, each containing a complete four-stage video (*i.e.*, saline, acetic acid, alcohol, and iodine) along with the corresponding stage keyframes and pathology report. The dataset covers a wide spectrum of cervical conditions, including normal tissues, low-grade lesions, and high-grade intraepithelial neoplasia. Each case is independently reviewed by three senior gynecologists, who delineate biopsy sites and verify pathological outcomes based on histopathological reports.

Metrics Performance is evaluated using four metrics: Recall, Precision, Accuracy, and Tolerant Recall (Recall@1). Recall@1 considers a prediction correct if it falls within one adjacent position of the true biopsy site, reflecting the clinically acceptable localization tolerance.

Table 1. **Quantitative results of fully supervised colposcopy video analysis on our in-house dataset.** Results are obtained through five-fold cross-validation. Recall@1 considers predictions within one adjacent position as correct. See Sec. 4.1 for details.

Category	Methods	Recall \uparrow	Precision \uparrow	Acc. \uparrow	Recall@1 \uparrow
<i>General</i>	TimeFormer _[ICML21] [3]	54.8	57.9	25.6	70.4
	VideoSwin _[CVPR22] [40]	60.9	61.8	29.7	75.2
	VideoMAEv2 _[CVPR23] [68]	65.3	65.9	33.5	77.6
<i>Medical</i>	VideoCutMix _[MICCAI24] [17]	67.3	68.2	39.8	81.5
	SurgFormer _[MICCAI24] [79]	70.1	66.8	41.2	82.8
	PolypSegTrack _[MICCAI25] [14]	65.5	63.8	36.5	79.6
	EchoPrime _[Nature25] [66]	67.8	66.1	37.4	80.2
	STDDNet _[ICCV25] [10]	66.8	67.1	38.1	82.3
	SurgVLP _[MIA25] [82]	68.9	65.9	38.7	82.0
MEDVCR (Ours)		80.3	74.4	55.0	93.0

Compared methods Comparisons are conducted using both general and medical video understanding models to extract spatiotemporal representations.

- *General methods.* Representative natural video understanding models, including TimeFormer [3], VideoSwin [40], and VideoMAEv2 [68], are used.
- *Medical methods.* Since colposcopy-specific models are underexplored, typical video encoders from surgical (SurgFormer [79] and VideoCutMix [17]), endoscopic (SurgVLP [82], PolypSegTrack [14], and STDDNet [10]), and ultrasound (EchoPrime [66]) domains are adopted for comparison.
- *Ours.* The acetic acid and iodine stages are chosen as s_t and s_{t+1} , consistent with clinical practice where physicians primarily rely on these two stages for assessment.

Quantitative results Results are reported in Tab. 1. (i) Directly applying general video understanding models yields limited performance (*i.e.*, 70.4% Recall@1 for TimeFormer [3]), revealing a substantial domain gap between natural videos and clinical examinations. (ii) Models fine-tuned on related medical domains achieve moderate gains (*i.e.*, 82.8% Recall@1 for SurgFormer [79]), suggesting that medical priors can generalize across clinical tasks. (iii) **MEDVCR** achieves the best overall performance with **93.0%** Recall@1, demonstrating strong clinical applicability in accurately localizing biopsy sites.

4.2. Weakly Supervised Medical Video Diagnosis

Weakly supervised medical video diagnosis involves learning from video-level diagnostic labels without frame-level supervision. In this setting, **MEDVCR** is evaluated on weakly supervised polyp-frame detection in colonoscopy.

Task description Colonoscopy serves as the primary technique for the early detection and prevention of colorectal cancer [20]. In clinical practice, a flexible endoscope equipped with a camera is inserted through the rectum to observe the mucosal surface of the colon in real time [7]. The procedure focuses on detecting polyps—abnormal tissue growths with malignant potential—which often appear transiently as the endoscope moves through the lumen.

Table 2. **Quantitative results of weakly supervised colonoscopy video analysis on the combined Kvasir [4] and LDPolypVideo [42] dataset.** Results are obtained through five-fold cross-validation. See Sec. 4.2 for details.

Category	Methods	AP \uparrow	AUC \uparrow
<i>General</i>	GCN-Ano _[ICCV19] [86]	75.4	92.1
	CLAWS _[ECCV20] [83]	80.4	95.6
	MIST _[CVPR21] [22]	72.9	94.5
	RTFM _[ICCV21] [61]	78.0	96.3
	UR-DMU _[AAAI23] [87]	79.3	93.7
<i>Medical</i>	CTMIL _[MICCAI22] [62]	86.6	98.4
	Endo-FM _[MICCAI23] [70]	89.2	97.6
	EchoPrime _[Nature25] [66]	75.7	92.4
	Fadmb _[PR25] [41]	92.2	99.4
	MEDVCR (Ours)	94.8	99.6

Colonoscopy video analysis aims to identify frames containing visible polyps within the entire video.

Dataset Experiments are conducted on a widely used colonoscopy video benchmark integrating the Hyper-Kvasir [4] and LDPolypVideo [42] datasets. The combined dataset contains over one million frames collected from routine screening procedures, covering diverse polyp appearances with varying sizes, shapes, and textures under different illumination and viewing conditions. Following standard protocols [62], the training set includes 61 videos without visible polyps and 102 videos containing polyps, while the test set comprises 30 and 60 videos, respectively. Training videos are annotated at the video level, whereas test videos provide frame-level labels for evaluation.

Metrics Following prior studies [62], frame-level results are evaluated using Area Under the Receiver Operating Characteristic curve (AUC) and AP.

Compared methods Both general and domain-specific methods are included for evaluation under the same setting.

- *General methods.* Weakly supervised video anomaly detection baselines from natural video domains, including GCN-Ano [86], CLAWS [83], MIST [22], RTFM [61], and UR-DMU [87], are used for comparison.
- *Medical methods.* Weakly supervised polyp detection approaches (*i.e.*, CTMIL [62] and Fadmb [41]), the endoscopic foundation model Endo-FM [70], and EchoPrime [66], a large-scale ultrasound model, are included.
- *Ours.* Each colonoscopy video is divided into 32 snippets of 16 frames as input, and DDP produces snippet-level scores that are propagated to all frames for evaluation.

Quantitative results Tab. 2 summarizes the results on the combined dataset. **MEDVCR** achieves **94.8%** AP, surpassing the previous best method (*i.e.*, Fadmb [41]) by 2.6%. This performance gain highlights the advantage of counterfactual reasoning in modeling subtle pathological

Table 3. **Ablation studies on key components under fully supervised (colposcopy) and weakly supervised (colonoscopy) settings.** Results are averaged over five-fold cross-validation. See Sec. 4.3 for details.

#	Component		Colposcopy	Colonoscopy
	CRs	DDP	Recall@1 \uparrow	AP \uparrow
1	\times	\times	77.9	82.8
2	\checkmark	\times	89.4	91.6
3	\times	\checkmark	80.2	85.5
4	\checkmark	\checkmark	93.0	94.8

dynamics under weak supervision.

4.3. Ablation Study and Visualization

Comprehensive ablation studies validate the effectiveness of each component across fully supervised (colposcopy) and weakly supervised (colonoscopy) settings.

Key component analysis Tab. 3 evaluates the contribution of the clinical rules (CRs, Sec. 3.2) and DDP strategy (Sec. 3.3) across two medical tasks. (i) Row #1 represents the baseline model containing only the medical video learner (Sec. 3.2), reflecting the performance achievable by fine-tuning a pretrained visual encoder (*i.e.*, I3D [8]). (ii) Row #1 vs. Row #2: introducing CRs notably improves performance across both tasks (*i.e.*, 77.9% \rightarrow **89.4%** in Recall@1 for colposcopy), indicating that clinical knowledge injection enhances representation quality. (iii) Row #1 vs. Row #3: DDP also contributes to improved diagnostic performance (*i.e.*, 82.8% \rightarrow **85.5%** in AP for colonoscopy), demonstrating the value of integrating counterfactual reasoning into prediction. (iv) Row #2 vs. Row #3: CRs outperform DDP across both tasks, particularly in colposcopy (*i.e.*, 80.2% \rightarrow **89.4%** in Recall@1), further underscoring the importance of clinical knowledge for diagnostic representation. (v) Row #4 yields the best overall results, confirming the complementary effects of CRs and DDP.

CG evaluation (Sec. 3.1) Fig. 3 presents representative counterfactual generation results across colposcopy and colonoscopy scenarios. For colposcopy (Fig. 3(a)), across the acetic-acid to iodine progression, CG generates benign and malignant hypotheses for each factual frame. Row 1 shows a benign case where the malignant hypothesis adds subtle yellow-rough textures at clinically plausible locations, revealing early malignant tendencies not visible in the original frame. Row 2 presents a malignant case where the benign hypothesis restores smooth epithelial appearance while preserving lighting and geometry. Row 3 depicts a case with widespread lesions where the benign hypothesis remains coherent and structure-preserving. For colonoscopy (Fig. 3(b)), CG synthesizes next-stage appearances conditioned on the current observation, generating both *w/o* and *w/* polyp outcomes while preserving temporal coherence and mucosal structure. Notably, Row 3 recon-

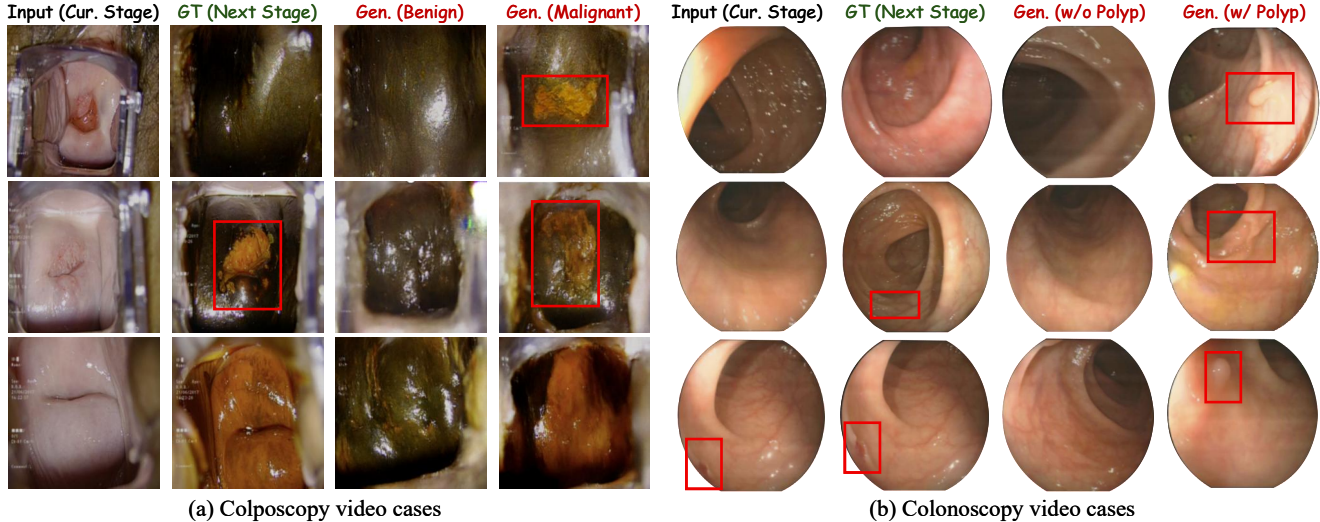


Figure 3. **Visualization of CG (Sec. 3.1) across two medical scenarios.** (a) Colposcopy: synthesizing reagent-induced tissue transitions across examination stages. (b) Colonoscopy: modeling temporal polyp emergence. Row 1: benign case; Rows 2&3: malignant cases.

Table 4. **Effectiveness of individual clinical rules (Sec. 3.2):** temporal consistency (Temp.), pathological separability (Sep.), and counterfactual alignment (Align.). Results are obtained through five-fold cross-validation. See Sec. 4.3 for details.

#	Clinical Rules			Colposcopy	Colonoscopy
	Temp.	Sep.	Align.	Recall@1↑	AP↑
1	✗	✗	✗	80.2	85.5
2	✓	✗	✗	84.1	88.0
3	✗	✓	✗	87.5	90.2
4	✗	✗	✓	90.8	93.0
5	✓	✓	✓	93.0	94.8

structs a complete polyp structure from an ulcerated surface, demonstrating anatomical reasoning beyond texture transformation.

CRL module assessment (Sec. 3.2) We further examine the influence of the CRL module on diagnostic performance.

Effectiveness of clinical rules. We first analyze the contribution of individual clinical rules within the CRL module. Tab. 4 shows that all three rules contribute positively to diagnostic performance across tasks. The counterfactual alignment rule provides the largest improvement (Row #1 vs. Row #4, 80.2%→**90.8%** in Recall@1 for colposcopy), demonstrating its critical role in linking factual and counterfactual representations for clinically coherent reasoning.

Effectiveness of visual encoder. We next evaluate the impact of different visual backbones in Tab. 5. Vision-language and self-supervised models show limited transferability to medical domains (*i.e.*, CLIP [52] achieves only 84.5% Recall@1 in colposcopy). Traditional CNN backbones yield moderate improvements (*i.e.*, ResNet101 [27] reaches 89.1% Recall@1). In contrast, video-based architectures exhibit the best overall performance, with I3D [8]

Table 5. **Effectiveness of different visual backbones within the medical video learner (Sec. 3.2).** Results are obtained through five-fold cross-validation. See Sec. 4.3 for details.

#	Backbone	Colposcopy	Colonoscopy
		Recall@1↑	AP↑
1	Ours (CLIP-ViT/B) _[ICML21] [52]	84.5	89.0
2	Ours (DINOv2-ViT/L) _[ICCV23] [49]	86.0	90.2
3	Ours (ResNet101) _[CVPR16] [27]	89.1	91.1
4	Ours (R(2+1)D) _[CVPR18] [63]	89.8	92.0
5	Ours (S3D) _[ECCV18] [73]	92.3	94.1
6	Ours (I3D) _[CVPR17] [8]	93.0	94.8

achieving the highest results (*i.e.*, **93.0%** Recall@1), underscoring the advantage of spatiotemporal modeling in capturing diagnostic progression.

5. Conclusion

This work presents **MEDVCR**, a counterfactual reasoning framework for medical video diagnosis that addresses key limitations of existing approaches. **MEDVCR** integrates three core components: a CG that synthesizes realistic tissue transitions under specified pathological states via diffusion modeling, a CRL module that enforces temporal consistency, pathological separability, and counterfactual alignment through clinically grounded rules, and a DDP strategy that combines global temporal context with frame-level counterfactual contrast. Extensive experiments on colposcopy (fully supervised) and colonoscopy (weakly supervised) demonstrate consistent improvements over all baselines, and comprehensive ablation studies verify the contribution of each component. We hope this work encourages further development of clinically grounded, interpretable diagnostic systems for medical video analysis.

References

- [1] Anurag Arnab, Mostafa Dehghani, Georg Heigold, Chen Sun, Mario Lučić, and Cordelia Schmid. Vivit: A video vision transformer. In *Proceedings of International Conference on Computer Vision (ICCV)*, 2021. 2
- [2] Maximilian Augustin, Yannic Neuhaus, and Matthias Hein. Dig-in: Diffusion guidance for investigating networks-uncovering classifier differences neuron visualisations and visual counterfactual explanations. In *Proceedings of Conference on Computer Vision and Pattern Recognition (CVPR)*, 2024. 2
- [3] Gedas Bertasius, Heng Wang, and Lorenzo Torresani. Is space-time attention all you need for video understanding? In *Proceedings of International Conference on Machine Learning (ICML)*, 2021. 6
- [4] Hanna Borgli, Vajira Thambawita, Pia H Smedsrud, Steven Hicks, Debesh Jha, Sigrun L Eskeland, Kristin Ranheim Randel, Konstantin Pogorelov, Mathias Lux, Duc Tien Dang Nguyen, et al. Hyperkvasir, a comprehensive multi-class image and video dataset for gastrointestinal endoscopy. *Scientific data*, 7(1):283, 2020. 7
- [5] Johann Brehmer, Pim De Haan, Phillip Lippe, and Taco S Cohen. Weakly supervised causal representation learning. In *Proceedings of Advances in Neural Information Processing Systems (NeurIPS)*, 2022. 2
- [6] Marc Brisson and Mélanie Drolet. Global elimination of cervical cancer as a public health problem. *The Lancet Oncology*, 20(3):319–321, 2019. 6
- [7] Qing Cao, Runyi Deng, Yue Pan, Ruijie Liu, Yicheng Chen, Guofang Gong, Jun Zou, Huayong Yang, and Dong Han. Robotic wireless capsule endoscopy: recent advances and upcoming technologies. *Nature Communications*, 15(1): 4597, 2024. 6
- [8] Joao Carreira and Andrew Zisserman. Quo vadis, action recognition? a new model and the kinetics dataset. In *Proceedings of Conference on Computer Vision and Pattern Recognition (CVPR)*, 2017. 2, 4, 5, 7, 8
- [9] Daniel C Castro, Ian Walker, and Ben Glocker. Causality matters in medical imaging. *Nature Communications*, 11(1): 3673, 2020. 2
- [10] Guilian Chen, Huisi Wu, and Jing Qin. Stddnet: Harnessing mamba for video polyp segmentation via spatial-aligned temporal modeling and discriminative dynamic representation learning. In *Proceedings of International Conference on Computer Vision (ICCV)*, 2025. 2, 6
- [11] Tingxiu Chen, Yilei Shi, Zixuan Zheng, Bingcong Yan, Jingliang Hu, Xiao Xiang Zhu, and Lichao Mou. Ultrasound image-to-video synthesis via latent dynamic diffusion models. In *International Conference on Medical Image Computing and Computer Assisted Intervention (MICCAI)*, 2024. 1
- [12] Zhen Chen, Qingyu Guo, Leo KT Yeung, Danny TM Chan, Zhen Lei, Hongbin Liu, and Jinqiao Wang. Surgical video captioning with mutual-modal concept alignment. In *International Conference on Medical Image Computing and Computer Assisted Intervention (MICCAI)*, 2023. 2
- [13] Yunjey Choi, Minje Choi, Muniyoung Kim, Jung-Woo Ha, Sunghun Kim, and Jaegul Choo. Stargan: Unified generative adversarial networks for multi-domain image-to-image translation. In *Proceedings of Conference on Computer Vision and Pattern Recognition (CVPR)*, 2018. 2
- [14] Anwesa Choudhuri, Zhongpai Gao, Meng Zheng, Benjamin Planche, Terrence Chen, and Ziyang Wu. Polypsegtrack: unified foundation model for colonoscopy video analysis. In *International Conference on Medical Image Computing and Computer Assisted Intervention (MICCAI)*, 2025. 1, 2, 6
- [15] Tobias Czempel, Magdalini Paschali, Daniel Ostler, Seong Tae Kim, Benjamin Busam, and Nassir Navab. Opera: Attention-regularized transformers for surgical phase recognition. In *International Conference on Medical Image Computing and Computer Assisted Intervention (MICCAI)*, 2021. 1, 2
- [16] Xiaolong Deng, Huisi Wu, Runhao Zeng, and Jing Qin. Memsam: Taming segment anything model for echocardiography video segmentation. In *Proceedings of Conference on Computer Vision and Pattern Recognition (CVPR)*, 2024. 2
- [17] Rohan Raju Dhanakshirur, Mrinal Tyagi, Britty Baby, Ashish Suri, Prem Kalra, and Chetan Arora. Videocutmix: Temporal segmentation of surgical videos in scarce data scenarios. In *International Conference on Medical Image Computing and Computer Assisted Intervention (MICCAI)*, 2024. 6
- [18] Neeraj Dhungel, Gustavo Carneiro, and Andrew P Bradley. The automated learning of deep features for breast mass classification from mammograms. In *International Conference on Medical Image Computing and Computer Assisted Intervention (MICCAI)*, 2016. A1
- [19] Xinpeng Ding and Xiaomeng Li. Exploring segment-level semantics for online phase recognition from surgical videos. *IEEE Transactions on Medical Imaging (TMI)*, 41(11):3309–3319, 2022. 2
- [20] Deng-Ping Fan, Ge-Peng Ji, Tao Zhou, Geng Chen, Huazhu Fu, Jianbing Shen, and Ling Shao. Pranel: Parallel reverse attention network for polyp segmentation. In *International Conference on Medical Image Computing and Computer Assisted Intervention (MICCAI)*, 2020. 6
- [21] Christoph Feichtenhofer, Haoqi Fan, Jitendra Malik, and Kaiming He. Slowfast networks for video recognition. In *Proceedings of International Conference on Computer Vision (ICCV)*, 2019. 2
- [22] Jia-Chang Feng, Fa-Ting Hong, and Wei-Shi Zheng. Mist: Multiple instance self-training framework for video anomaly detection. In *Proceedings of Conference on Computer Vision and Pattern Recognition (CVPR)*, 2021. 7
- [23] Xiaojie Gao, Yueming Jin, Yonghao Long, Qi Dou, and Pheng-Ann Heng. Trans-svnet: Accurate phase recognition from surgical videos via hybrid embedding aggregation transformer. In *International Conference on Medical Image Computing and Computer Assisted Intervention (MICCAI)*, pages 593–603, 2021. 1
- [24] Lore Goetschalckx, Alex Andonian, Aude Oliva, and Phillip Isola. Ganalyze: Toward visual definitions of cognitive image properties. In *Proceedings of International Conference on Computer Vision (ICCV)*, 2019. 2
- [25] Xiaoqing Guo, Qianhui Men, and J Alison Noble. Mmsummary: Multimodal summary generation for fetal ultrasound

- video. In *International Conference on Medical Image Computing and Computer Assisted Intervention (MICCAI)*, 2024. 1
- [26] Michaela T Hall, Kate T Simms, John M Murray, Adam Keane, Diep TN Nguyen, Michael Caruana, Gigi Lui, Helen Kelly, Linda O Eckert, Nancy Santesso, et al. Benefits and harms of cervical screening, triage and treatment strategies in women living with hiv. *Nature Medicine*, 29(12): 3059–3066, 2023. 1, A1
- [27] Kaiming He, Xiangyu Zhang, Shaoqing Ren, and Jian Sun. Deep residual learning for image recognition. In *Proceedings of Conference on Computer Vision and Pattern Recognition (CVPR)*, 2016. 8, A1
- [28] Wenyi Hong, Yean Cheng, Zhuoyi Yang, Weihang Wang, Lefan Wang, Xiaotao Gu, Shiyu Huang, Yuxiao Dong, and Jie Tang. Motionbench: Benchmarking and improving fine-grained video motion understanding for vision language models. In *Proceedings of Conference on Computer Vision and Pattern Recognition (CVPR)*, 2025. 1
- [29] Ming Hu, Lin Wang, Siyuan Yan, Don Ma, Qingli Ren, Peng Xia, Wei Feng, Peibo Duan, Lie Ju, and Zongyuan Ge. Nurvid: A large expert-level video database for nursing procedure activity understanding. In *Proceedings of Advances in Neural Information Processing Systems (NeurIPS)*, 2023. 1
- [30] Shih-Cheng Huang, Anuj Pareek, Malte Jensen, Matthew P Lungren, Serena Yeung, and Akshay S Chaudhari. Self-supervised learning for medical image classification: a systematic review and implementation guidelines. *NPJ Digital Medicine*, 6(1):74, 2023. 2
- [31] Adrián Javaloy, Pablo Sánchez-Martín, and Isabel Valera. Causal normalizing flows: from theory to practice. In *Proceedings of Advances in Neural Information Processing Systems (NeurIPS)*, 2023. 2
- [32] Guillaume Jeanneret, Loïc Simon, and Frédéric Jurie. Adversarial counterfactual visual explanations. In *Proceedings of Conference on Computer Vision and Pattern Recognition (CVPR)*, 2023. 2
- [33] Yueming Jin, Qi Dou, Hao Chen, Lequan Yu, Jing Qin, Chi-Wing Fu, and Pheng-Ann Heng. Sv-rcnet: workflow recognition from surgical videos using recurrent convolutional network. *IEEE Transactions on Medical Imaging (TMI)*, 37(5): 1114–1126, 2017. 2
- [34] Yueming Jin, Huaxia Li, Qi Dou, Hao Chen, Jing Qin, Chi-Wing Fu, and Pheng-Ann Heng. Multi-task recurrent convolutional network with correlation loss for surgical video analysis. *Medical Image Analysis (MIA)*, 59:101572, 2020. 2
- [35] Smita Joshi, Richard Muwonge, Ramesh Bhosale, Pritam Chaudhari, Vinay Kulkarni, Mahesh Mandolkar, Kedar Deodhar, Seema Kand, Nikhil Phadke, Shobini Rajan, et al. A randomised controlled non-inferiority trial to compare the efficacy of ‘hvp screen, triage and treat’ with ‘hvp screen and treat’ approach for cervical cancer prevention among women living with hiv. *Nature Communications*, 16(1):1888, 2025. 1, A1
- [36] Siwon Kim, Jinoh Oh, Sungjin Lee, Seunghak Yu, Jaeyoung Do, and Tara Taghavi. Grounding counterfactual explanation of image classifiers to textual concept space. In *Proceedings of Conference on Computer Vision and Pattern Recognition (CVPR)*, 2023. 2
- [37] Xiaodi Li, Chen Cui, Siyuan Shi, Hongwen Fei, and Yue Hu. Semi-supervised echocardiography video segmentation via adaptive spatio-temporal tensor semantic awareness and memory flow. *IEEE Transactions on Medical Imaging (TMI)*, 2025. 2
- [38] Haohong Lin, Xin Huang, Tung Phan, David Hayden, Huan Zhang, Ding Zhao, Siddhartha Srinivasa, Eric Wolff, and Hongge Chen. Causal composition diffusion model for closed-loop traffic generation. In *Proceedings of Conference on Computer Vision and Pattern Recognition (CVPR)*, 2025. 2
- [39] Yang Liu, Jiayu Huo, Jingjing Peng, Rachel Sparks, Prokar Dasgupta, Alejandro Granados, and Sebastien Ourselin. Skit: a fast key information video transformer for online surgical phase recognition. In *Proceedings of International Conference on Computer Vision (ICCV)*, 2023. 1
- [40] Ze Liu, Jia Ning, Yue Cao, Yixuan Wei, Zheng Zhang, Stephen Lin, and Han Hu. Video swin transformer. In *Proceedings of Conference on Computer Vision and Pattern Recognition (CVPR)*, 2022. 6
- [41] Zhiming Luo, Shuheng Huang, Kun Yang, Jianzhe Gao, and Shaozi Li. Fadmb: Fully attention-based dual memory bank network for weakly supervised video anomaly detection. In *Pattern Recognition (PR)*, 2025. 7
- [42] Yiting Ma, Xuejin Chen, Kai Cheng, Yang Li, and Bin Sun. Ldpolypvideo benchmark: a large-scale colonoscopy video dataset of diverse polyps. In *International Conference on Medical Image Computing and Computer Assisted Intervention (MICCAI)*, 2021. 1, 7
- [43] Yuchen Ma, Valentyn Melnychuk, Jonas Schweisthal, and Stefan Feuerriegel. Diffpo: A causal diffusion model for learning distributions of potential outcomes. In *Proceedings of Advances in Neural Information Processing Systems (NeurIPS)*, 2024. 2
- [44] Neelu Madan, Nicolae-Cătălin Ristea, Radu Tudor Ionescu, Kamal Nasrollahi, Fahad Shahbaz Khan, Thomas B Moeslund, and Mubarak Shah. Self-supervised masked convolutional transformer block for anomaly detection. *Transactions on Pattern Analysis and Machine Intelligence (TPAMI)*, 46(1):525–542, 2023. 2
- [45] Thomas Melistas, Nikos Spyrou, Nefeli Gkouti, Pedro Sanchez, Athanasios Vlontzos, Yannis Panagakis, Giorgos Papanastasiou, and Sotirios A Tsaftaris. Benchmarking counterfactual image generation. In *Proceedings of Advances in Neural Information Processing Systems (NeurIPS)*, 2024. 2
- [46] Divyanshu Mishra, Pramit Saha, He Zhao, Netzahualcoyotl Hernandez-Cruz, Olga Patey, Aris Papageorghiou, and J Alison Noble. Mcat: Visual query-based localization of standard anatomical clips in fetal ultrasound videos using multi-tier class-aware token transformer. In *Proceedings of AAAI Conference on Artificial Intelligence (AAAI)*, 2025. 1
- [47] Divyanshu Mishra, Pramit Saha, He Zhao, Netzahualcoyotl Hernandez-Cruz, Olga Patey, Aris T Papageorghiou, and

- J Alison Noble. Tier-loc: Visual query-based video clip localization in fetal ultrasound videos with a multi-tier transformer. *Medical Image Analysis (MIA)*, page 103611, 2025. 2
- [48] Inês C Moreira, Igor Amaral, Inês Domingues, António Cardoso, Maria Joao Cardoso, and Jaime S Cardoso. Inbreast: toward a full-field digital mammographic database. *Academic radiology*, 19(2):236–248, 2012. A1
- [49] Maxime Oquab, Timothée Darcet, Théo Moutakanni, Huy V. Vo, Marc Szafraniec, Vasil Khalidov, Pierre Fernandez, Daniel HAZIZA, Francisco Massa, Alaaeldin El-Nouby, Mido Assran, Nicolas Ballas, Wojciech Galuba, Russell Howes, Po-Yao Huang, Shang-Wen Li, Ishan Misra, Michael Rabbat, Vasu Sharma, Gabriel Synnaeve, Hu Xu, Herve Jegou, Julien Mairal, Patrick Labatut, Armand Joulin, and Piotr Bojanowski. DINOv2: Learning robust visual features without supervision. *Transactions on Machine Learning Research (TMLR)*, 2024. 8
- [50] Zhenghao Pan, Haijin Zeng, Jiezhong Cao, Yongyong Chen, Kai Zhang, and Yong Xu. Mambasci: Efficient mamba-unet for quad-bayer patterned video snapshot compressive imaging. In *Proceedings of Advances in Neural Information Processing Systems (NeurIPS)*, 2024. 1
- [51] Nick Pawlowski, Daniel Coelho de Castro, and Ben Glocker. Deep structural causal models for tractable counterfactual inference. In *Proceedings of Advances in Neural Information Processing Systems (NeurIPS)*, 2020. 2
- [52] Alec Radford, Jong Wook Kim, Chris Hallacy, Aditya Ramesh, Gabriel Goh, Sandhini Agarwal, Girish Sastry, Amanda Askell, Pamela Mishkin, Jack Clark, et al. Learning transferable visual models from natural language supervision. In *Proceedings of International Conference on Machine Learning (ICML)*, 2021. 8
- [53] Jonathan G Richens, Ciarán M Lee, and Saurabh Johri. Improving the accuracy of medical diagnosis with causal machine learning. *Nature communications*, 11(1):3923, 2020. 2
- [54] Dominik Rivoir, Isabel Funke, and Stefanie Speidel. On the pitfalls of batch normalization for end-to-end video learning: a study on surgical workflow analysis. *Medical Image Analysis (MIA)*, 94:103126, 2024. 2
- [55] Lena Schreiberhuber, James E Barrett, Jiangrong Wang, Elisa Redl, Chiara Herzog, Charlotte D Vavourakis, Karin Sundström, Joakim Dillner, and Martin Widschwendter. Cervical cancer screening using dna methylation triage in a real-world population. *Nature medicine*, 30(8):2251–2257, 2024. 1, A1
- [56] Wenhao Shen, Mingliang Zhou, Yu Chen, Xuekai Wei, Yong Feng, Huayan Pu, and Weijia Jia. Image quality assessment: Investigating causal perceptual effects with abductive counterfactual inference. In *Proceedings of Conference on Computer Vision and Pattern Recognition (CVPR)*, 2025. 2
- [57] Jascha Sohl-Dickstein, Eric Weiss, Niru Maheswaranathan, and Surya Ganguli. Deep unsupervised learning using nonequilibrium thermodynamics. In *International conference on machine learning*, pages 2256–2265. pmlr, 2015. 3
- [58] Xue Song, Jiequan Cui, Hanwang Zhang, Jingjing Chen, Richang Hong, and Yu-Gang Jiang. Doubly abductive counterfactual inference for text-based image editing. In *Proceedings of Conference on Computer Vision and Pattern Recognition (CVPR)*, 2024. 2
- [59] Ryan W Stidham, Lingrui Cai, Shuyang Cheng, Flora Rajaei, Tadd Hiatt, Emily Wittrup, Michael D Rice, Shrinivas Bishu, Jan Wehkamp, Weiwei Schultz, et al. Using computer vision to improve endoscopic disease quantification in therapeutic clinical trials of ulcerative colitis. *Gastroenterology*, 166(1): 155–167, 2024. 1
- [60] Rong Tao, Xiaoyang Zou, and Guoyan Zheng. Last: Latent space-constrained transformers for automatic surgical phase recognition and tool presence detection. *IEEE Transactions on Medical Imaging (TMI)*, 42(11):3256–3268, 2023. 2
- [61] Yu Tian, Guansong Pang, Yuanhong Chen, Rajvinder Singh, Johan W Verjans, and Gustavo Carneiro. Weakly-supervised video anomaly detection with robust temporal feature magnitude learning. In *Proceedings of International Conference on Computer Vision (ICCV)*, 2021. 7
- [62] Yu Tian, Guansong Pang, Fengbei Liu, Yuyuan Liu, Chong Wang, Yuanhong Chen, Johan Verjans, and Gustavo Carneiro. Contrastive transformer-based multiple instance learning for weakly supervised polyp frame detection. In *International Conference on Medical Image Computing and Computer Assisted Intervention (MICCAI)*, 2022. 2, 7
- [63] Du Tran, Heng Wang, Lorenzo Torresani, Jamie Ray, Yann LeCun, and Manohar Paluri. A closer look at spatiotemporal convolutions for action recognition. In *Proceedings of Conference on Computer Vision and Pattern Recognition (CVPR)*, 2018. 8
- [64] Andru P Twinanda, Sherif Shehata, Didier Mutter, Jacques Marescaux, Michel De Mathelin, and Nicolas Padoy. Endonet: a deep architecture for recognition tasks on laparoscopic videos. *IEEE Transactions on Medical Imaging (TMI)*, 36(1):86–97, 2016. 2
- [65] Andru Putra Twinanda, Gaurav Yengera, Didier Mutter, Jacques Marescaux, and Nicolas Padoy. Rsdnet: Learning to predict remaining surgery duration from laparoscopic videos without manual annotations. *IEEE Transactions on Medical Imaging (TMI)*, 38(4):1069–1078, 2018. 2
- [66] Milos Vukadinovic, Xiu Tang, Neal Yuan, Paul Cheng, Debiao Li, Susan Cheng, Bryan He, and David Ouyang. Comprehensive echocardiogram evaluation with view primed vision language ai. *Nature*, 2025. 6, 7
- [67] Churan Wang, Jing Li, Fandong Zhang, Xinwei Sun, Hao Dong, Yizhou Yu, and Yizhou Wang. Bilateral asymmetry guided counterfactual generating network for mammogram classification. *Transactions on Image Processing (TIP)*, 30: 7980–7994, 2021. 2, A1
- [68] Limin Wang, Bingkun Huang, Zhiyu Zhao, Zhan Tong, Yinan He, Yi Wang, Yali Wang, and Yu Qiao. Videomae v2: Scaling video masked autoencoders with dual masking. In *Proceedings of Conference on Computer Vision and Pattern Recognition (CVPR)*, 2023. 6
- [69] Shihao Wang, Zhiding Yu, Xiaohui Jiang, Shiyi Lan, Min Shi, Nadine Chang, Jan Kautz, Ying Li, and Jose M Alvarez. Omnidrive: A holistic vision-language dataset for autonomous driving with counterfactual reasoning. In *Proceed-*

- ings of *Conference on Computer Vision and Pattern Recognition (CVPR)*, 2025. 2
- [70] Zhao Wang, Chang Liu, Shaoting Zhang, and Qi Dou. Foundation model for endoscopy video analysis via large-scale self-supervised pre-train. In *International Conference on Medical Image Computing and Computer Assisted Intervention (MICCAI)*, 2023. 2, 7
- [71] Nan Wu, Jason Phang, Jungkyu Park, Yiqiu Shen, Zhe Huang, Masha Zorin, Stanisław Jastrzebski, Thibault Févry, Joe Katsnelson, Eric Kim, et al. Deep neural networks improve radiologists’ performance in breast cancer screening. *IEEE Transactions on Medical Imaging (TMI)*, 39(4):1184–1194, 2019. A1
- [72] Yao Xiao, Ziyi Tang, Pengxu Wei, Cong Liu, and Liang Lin. Masked images are counterfactual samples for robust fine-tuning. In *Proceedings of Conference on Computer Vision and Pattern Recognition (CVPR)*, 2023. 2
- [73] Saining Xie, Chen Sun, Jonathan Huang, Zhuowen Tu, and Kevin Murphy. Rethinking spatiotemporal feature learning: Speed-accuracy trade-offs in video classification. In *Proceedings of European Conference on Computer Vision (ECCV)*, 2018. 8
- [74] Xiaozheng Xie, Jianwei Niu, Xuefeng Liu, Zhengsu Chen, Shaojie Tang, and Shui Yu. A survey on incorporating domain knowledge into deep learning for medical image analysis. *Medical Image Analysis (MIA)*, 69:101985, 2021. 2
- [75] Hanwen Xu, Naoto Usuyama, Jaspreet Bagga, Sheng Zhang, Rajesh Rao, Tristan Naumann, Cliff Wong, Zelalem Gero, Javier González, Yu Gu, et al. A whole-slide foundation model for digital pathology from real-world data. *Nature*, 630(8015):181–188, 2024. 2
- [76] Peng Xue, Le Dang, Ling-Hua Kong, Hong-Ping Tang, Hai-Miao Xu, Hai-Yan Weng, Zhe Wang, Rong-Gan Wei, Lian Xu, Hong-Xia Li, et al. Deep learning enabled liquid-based cytology model for cervical precancer and cancer detection. *Nature Communications*, 16(1):3506, 2025. 6, A1
- [77] Mengyue Yang, Furu Liu, Zhitang Chen, Xinwei Shen, Jianye Hao, and Jun Wang. Causalvae: Structured causal disentanglement in variational autoencoder. In *Proceedings of Conference on Computer Vision and Pattern Recognition (CVPR)*, 2021. 2
- [78] Mengyue Yang, Furu Liu, Zhitang Chen, Xinwei Shen, Jianye Hao, and Jun Wang. Causalvae: Disentangled representation learning via neural structural causal models. In *Proceedings of Conference on Computer Vision and Pattern Recognition (CVPR)*, 2021. 2
- [79] Shu Yang, Luyang Luo, Qiong Wang, and Hao Chen. Surgformer: Surgical transformer with hierarchical temporal attention for surgical phase recognition. In *International Conference on Medical Image Computing and Computer Assisted Intervention (MICCAI)*, 2024. 2, 6
- [80] Yijun Yang, Zhaohu Xing, Lequan Yu, Chunwang Huang, Huazhu Fu, and Lei Zhu. Vivim: A video vision mamba for medical video segmentation. *IEEE Transactions on Circuits and Systems for Video Technology (TCSVT)*, 2025. 1, 2
- [81] Yousef Yeganeh, Azade Farshad, Ioannis Charisiadis, Marta Hasny, Martin Hartenberger, Björn Ommer, Nassir Navab, and Ehsan Adeli. Latent drifting in diffusion models for counterfactual medical image synthesis. In *Proceedings of Conference on Computer Vision and Pattern Recognition (CVPR)*, 2025. 2
- [82] Kun Yuan, Vinkle Srivastav, Tong Yu, Joel L Lavanchy, Jacques Marescaux, Pietro Mascagni, Nassir Navab, and Nicolas Padoy. Learning multi-modal representations by watching hundreds of surgical video lectures. *Medical Image Analysis (MIA)*, page 103644, 2025. 6
- [83] Muhammad Zaigham Zaheer, Arif Mahmood, Marcella Astrid, and Seung-Ik Lee. Claws: Clustering assisted weakly supervised learning with normalcy suppression for anomalous event detection. In *Proceedings of European Conference on Computer Vision (ECCV)*, 2020. 7
- [84] Mingkun Zhang, Keping Bi, Wei Chen, Quanrun Chen, Jiafeng Guo, and Xueqi Cheng. Causaldiff: Causality-inspired disentanglement via diffusion model for adversarial defense. In *Proceedings of Advances in Neural Information Processing Systems (NeurIPS)*, 2024. 2
- [85] Sheng Zhang, Yanbo Xu, Naoto Usuyama, Hanwen Xu, Jaspreet Bagga, Robert Tinn, Sam Preston, Rajesh Rao, Mu Wei, Naveen Valluri, et al. A multimodal biomedical foundation model trained from fifteen million image–text pairs. *Nejm Ai*, 2(1):A10a2400640, 2025. 2
- [86] Jia-Xing Zhong, Nannan Li, Weijie Kong, Shan Liu, Thomas H Li, and Ge Li. Graph convolutional label noise cleaner: Train a plug-and-play action classifier for anomaly detection. In *Proceedings of Conference on Computer Vision and Pattern Recognition (CVPR)*, 2019. 7
- [87] Hang Zhou, Junqing Yu, and Wei Yang. Dual memory units with uncertainty regulation for weakly supervised video anomaly detection. In *Proceedings of AAAI Conference on Artificial Intelligence (AAAI)*, 2023. 7
- [88] Bin Zhu and Chong-Wah Ngo. Cookgan: Causality based text-to-image synthesis. In *Proceedings of Conference on Computer Vision and Pattern Recognition (CVPR)*, 2020. 2
- [89] Wentao Zhu, Qi Lou, Yeeleng Scott Vang, and Xiaohui Xie. Deep multi-instance networks with sparse label assignment for whole mammogram classification. In *International Conference on Medical Image Computing and Computer Assisted Intervention (MICCAI)*, 2017. A1
- [90] Odysseas Zisimopoulos, Evangello Flouty, Imanol Luengo, Petros Giataganas, Jean Nehme, Andre Chow, and Danail Stoyanov. Deepphase: surgical phase recognition in cataracts videos. In *International Conference on Medical Image Computing and Computer Assisted Intervention (MICCAI)*, 2018. 2

A. Additional Details about Colposcopy

A.1. Task Description

Colposcopy is a standard procedure for cervical cancer screening, where the cervix is inspected under sequential reagent applications—saline, acetic acid, alcohol, and iodine—to reveal tissue responses indicative of underlying pathology [55]. During the examination, gynecologists determine biopsy sites, *i.e.*, specific anatomical regions from which tissue samples are taken for histopathological confirmation [76]. Clinically, the cervix is divided into **12 clock-position regions**, and each region may contain one or more suspicious lesions [26]. Expert colposcopists assess reagent-induced color and texture changes such as acetowhitening, mosaicism, punctation, and iodine-negative areas [35]. Among these stages, the transition from acetic-acid reaction to iodine staining provides the most discriminative cues for identifying pathological regions and is therefore the primary basis for biopsy-site localization, as shown in Fig. A1. Accordingly, the task is formulated as a multi-label classification problem that predicts biopsy-site locations from the full multi-stage colposcopy video.

A.2. Training Details

Each examination contains a four-stage colposcopy video. For temporal modeling, the full sequence is divided into overlapping 16-frame clips using a temporal stride of 8. The overlap preserves smooth temporal continuity across stages and ensures that reagent-induced tissue changes are consistently captured for representation learning.

B. Additional Experiment

To assess the generalization ability of **MEDVCR** beyond video-based diagnosis, we evaluate it on a static imaging task, *i.e.*, bilateral mammography classification.

B.1. Mammography Image Analysis

Task description Mammography is the primary imaging technique for breast cancer screening and diagnosis [67]. This experiment is designed to verify the generalization capability of the proposed counterfactual reasoning framework. The breasts exhibit natural bilateral symmetry, where lesions on one side rarely appear in the corresponding



Figure A1. **Illustration of colposcopic biopsy-site determination.** By comparing tissue responses between the acetic-acid and iodine stages, clinicians localize suspicious areas on the cervix (organized into clock-position regions) for targeted biopsy sampling.

Table A1. **Quantitative results of mammography image analysis on INBreast [48].** Results are obtained through five-fold cross-validation. See Sec. B.1 for details.

Category	Methods	AUC \uparrow
<i>General</i>	ResNet50 _[CVPR16] [27]	69.0
	CNN-based _[MICCAI16] [18]	76.0
<i>Breast-specific</i>	Zhu <i>et al.</i> _[MICCAI17] [89]	86.0
	Wu <i>et al.</i> _[TMI19] [71]	86.3
	Wang <i>et al.</i> _[TIP21] [67]	90.9
MEDVCR (Ours)		93.4

region of the opposite breast [89]. Therefore, radiologists identify potential malignancies by examining asymmetries between paired views. This task involves detecting pathological lesions based on paired mammograms.

Dataset Experiments are performed on the public INBreast dataset [48], a high-quality benchmark for mammogram analysis. The dataset encompasses diverse lesion types, including masses, calcifications, and architectural distortions, representing challenging clinical scenarios. It contains 410 mammograms from 115 cases, each with paired left–right views and image-level BI-RADS annotations verified by pathological examination. Following standard practice [67], images are labeled as malignant if BI-RADS > 3 , and benign otherwise. For bilateral analysis, 91 valid left–right pairs are used for five-fold cross-validation.

Metrics Performance is evaluated using AUC, following [67].

Compared methods Bilateral mammogram analysis is formulated as a binary classification task. Evaluation involves three categories of representative methods.

- *General methods.* General image classification backbones, *i.e.*, ResNet50 [27] and CNN-based method [18], are employed as standard discriminative baselines.
- *Breast-specific methods.* These methods explicitly model bilateral breast symmetry for classification, including Zhu *et al.* [89], Wu *et al.* [71], and Wang *et al.* [67].
- *Ours.* The proposed framework is adapted for mammography by removing \mathcal{F}^t and retaining only \mathcal{F}^e , which independently processes each mammogram image.

Quantitative results Results on INBreast [48] are presented in Tab. A1. **MEDVCR** significantly surpasses the previous best method, Wang *et al.* [67] (*e.g.*, 90.9% \rightarrow **93.4%** in AUC). This demonstrates that our framework generalizes effectively to medical image analysis, validating its versatility across different clinical imaging modalities.

Qualitative results To further examine the behavior of the CG on static imaging, Fig. A2 presents qualitative results on malignant mammograms. For each malignant input (left), the generator produces a benign counterfactual hypothesis (middle). For reference, we also show the true contralateral breast (right), which is typically benign.

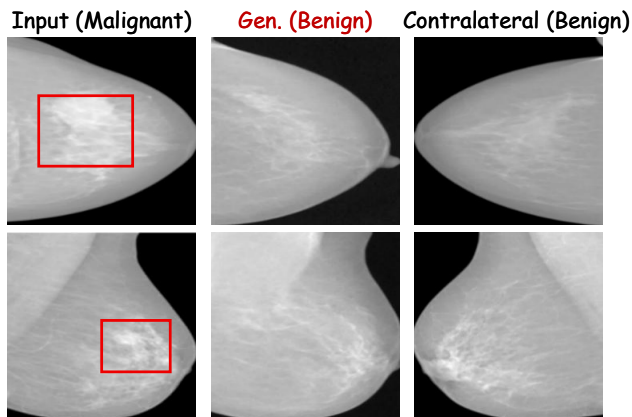


Figure A2. **Visualization of mammography counterfactuals.** Given a malignant input (left), the model generates a benign hypothesis (middle), which closely aligns with the appearance of the true contralateral breast (right). See Sec. B.1 for details.

The generated benign counterfactual suppresses malignant high-density regions and restores coherent glandular and parenchymal patterns. Its morphology resembles the true contralateral breast, demonstrating that our generator preserves global breast architecture while selectively removing pathology-specific structural abnormalities.

C. Discussion

Limitations and future work (i) *Scope of generative modeling.* Our CG is trained only to model short-range transitions between adjacent clinical stages. Its ability to synthesize longer-term or cross-stage evolution has not been evaluated and may limit applicability to procedures with complex temporal dynamics. (ii) *Coverage of clinical knowledge.* The clinical rules incorporated in **MEDVCR** reflect key diagnostic principles but do not encompass the full range of reasoning strategies used by experienced clinicians. Additional domain knowledge or adaptive rule learning may further improve representation fidelity. (iii) *Generality across modalities and institutions.* Although the framework shows strong performance across colposcopy, colonoscopy, and mammography, broader validation on multi-center datasets and diverse imaging modalities is necessary to assess the robustness of **MEDVCR**.

Broader impact This work explores the potential of counterfactual reasoning for medical video diagnosis. By generating clinically plausible benign–malignant hypotheses and explicitly modeling temporal tissue transitions, **MEDVCR** provides more transparent and clinically aligned diagnostic cues than conventional end-to-end methods. We hope this work encourages further development of clinically grounded, interpretable diagnostic systems for medical video analysis.